Nanoscale Advances

ROYAL SOCIETY OF CHEMISTRY

PAPER

View Article Online
View Journal

Check for updates

Cite this: DOI: 10.1039/d5na01087j

# Real-time optical spectroscopy for *in situ* single-droplet analysis

Rama Pandillapally,[a] Pillanagrovi Jayakumar,[b] Shourya Dutta-Gupta *[b] and Suhanya Duraiswamy *[a]

Received 22nd November 2025
Accepted 19th January 2026

DOI: 10.1039/d5na01087j

rsc.li/nanoscale-advances

*In situ* monitoring of chemical reactions, specifically reactions leading to the formation of plasmonic nanomaterials within droplets, has become a necessity for several applications in nanotechnology and sensing. In this study, we use a custom-designed optical transmission spectroscopy setup that can detect signals from a single anisotropic droplet over the entire visible spectral range (400–900 nm) without the use of external additives as reporters. We use data obtained from light scattered by the droplets to differentiate the 'drop only' regions from the 'oil only' regions and to extract information from within single droplets. We then load the droplets with anisotropic gold nanoparticles of different concentrations and show the variations in the optical signals based on their concentrations from single droplets and compare the data to the averaged data from several droplets, to demonstrate the validity of our technique. Finally, we employ the developed platform for monitoring *in situ* synthesis of gold nanoparticles within a microfluidic chip in real-time. Measurement at different locations along the channel enables us to track the reaction within a droplet at different time points, providing insights into the reaction kinetics. We also measure spectral data to understand the influence of reagent concentration on the synthesis. The developed technique can thus be employed for *in situ* monitoring of any chemical reaction within a single anisotropic droplet, provided it has absorption/transmission signatures, and will find wide applicability in the development of single-droplet analysis platforms.

## Introduction

Droplet microfluidics involves the controlled formation and transport of nanolitre to picolitre-sized droplets in an immiscible phase (typically oil) and is often used in applications involving highly parallelized and precise measurements.[1] Typically, droplets are employed as micro-controlled reactors (reaction/assay chambers) as each miniaturized droplet (lengths ~ nm to μm) can be regulated and operated independently.[2–4] A pump-controlled reagent dispensing procedure imparts precise control over the reagent volumes in individual droplets, as it is automated; meanwhile, chaotic advection within each droplet enables identical mixing patterns within them, thus ensuring robust and reproducible assays with improved reaction kinetics and without significant batch-to-batch variations.[5] The current research focus in the droplet microfluidics arena is on building capabilities to independently manipulate and monitor each droplet, which will, in turn, enable the identification of reaction mechanisms, crystal structures and biochemical pathways leading to pathological and physiological changes in cells,[6] tissues and/or organs.

Real-time monitoring of individual droplets and recognizing variations in successive droplets over time is a significant challenge. Real-time monitoring provides vital information about reaction mechanisms and biochemical pathways and can also be used to modify and manipulate parameters effectively and efficiently to achieve desired results. Researchers have explored various approaches for real-time monitoring by integrating mass spectroscopy,[7] electrochemical,[8] and optical[9] platforms with microchannels to analyse individual droplets over a period of time. Each method of monitoring has its advantages and limitations. For example, when using electrochemical monitoring techniques, measuring the presence of small molecules like $H_2O_2$ by appropriate coupling with a redox reaction is possible. However, in this case, the microfluidic device must be integrated with electrodes to carry out electrical measurements. Conversely, mass spectroscopic approaches provide unparalleled sensitivity and specificity, owing to the unique signatures observed in the mass spectrum. However, this is a destructive technique that results in loss of the prepared sample. In contrast, monitoring single droplets through their optical signatures opens up avenues for non-destructive and non-invasive detection of various species in the droplet. Optical interrogation techniques of a droplet have

---

[a] *Chemical Engineering, Indian Institute of Technology Hyderabad, Sangareddy 502284, Telangana, India. E-mail: suhanya@che.iith.ac.in*

[b] *Materials Science and Metallurgical Engineering, Indian Institute of Technology Hyderabad, Sangareddy 502284, Telangana, India. E-mail: shourya@msme.iith.ac.in*

been used for single-cell analysis, biochemical analysis, molecular detection, and cell sorting[10,11] due to their high sensitivity, fast response, and ease of integration with microreactors.[12]

Optical interrogation techniques deal with methods where light is absorbed, emitted, or dispersed by a sample (a droplet in this case or a sample within the droplet) to access its properties, such as composition, structure, and electrical and/or vibrational properties.[13–18] In such cases, the microfluidic chip is integrated with optical components directly by aligning the optical path with the channel through which droplets flow and the detector collects the signals, which are processed to obtain the corresponding signatures. Optical interrogation can be performed by monitoring modulations in optical signals (like transmission, absorption, scattering, fluorescence and Raman scattering) as a function of flow parameters within a single droplet.[19,20] Raman and fluorescence spectroscopy techniques have been integrated with droplet microfluidics to carry out single-droplet analysis.[21–24] For example, Cecchini *et al.* reported the aggregation of silver nanoparticles in droplet microfluidics using the Raman reporter malachite green (MG) with an exposure time of 10 μs,[25,26] while fluorescence detection methods have been reported by Casadevall*et al.*[23] Both of these methods capture inelastically scattered signals, and high signal-to-noise (S/N) ratios are possible due to efficient filtering using filter cubes. However, in both of these cases, a Raman reporter or a fluorescing molecule needs to be added to the aqueous solution to enable detection.[27,28]

Several absorbance-based detectors have been reported in the literature for glucose detection, single-cell analysis and enzymatic reactions.[29–31] However, these methods are limited to the study of large droplets due to the inherent short optical pathlength at the single-droplet level. This limitation has been addressed recently: Duncombe *et al.* demonstrated an UV-vis absorption spectrum-based droplet sorter wherein they acquired a broadband spectrum (200–1050 nm) at 2100 spectra per second in a microchip. Their devices had implanted waveguides (optical fiber inserted on either side of the region of interest), enabling excellent spatial and temporal localized measurements within the channels. However, this configuration limits the ability to choose the point of interrogation along the channel length, restricting the use of the proposed detection scheme for time-dependent processes, such as reaction kinetics analysis.[32]

Probst *et al.* established a sensitive technique that was able to acquire complete absorption spectra from a single pL droplet by using a fast spectrometer for integration times as short as 50 μs per spectrum. Additionally, they also used a postprocessing algorithm that improves the (S/N) ratio by removing the spectrum of the oil (by using a single wavelength time trace at 405 nm, as the fluorinated oil had a higher absorbance than the aqueous phase). They then examined the salt-induced aggregation of spherical nanoparticles in single spherical droplets. They initially used fluorescein isothiocyanate to test their method and were able to determine 800 nM concentrations of the fluorescent molecule in the droplets.[33] They then used the same technique to show the detection of spherical gold nanoparticles (GNPs) in the droplets. The reported method was used for measuring the signatures of preformed GNPs (off-chip synthesis) in spherical droplets, and their salt-induced aggregations.

Sulliger *et al.* recently proposed an optofluidic platform consisting of hyperspectral imaging (HSI) using a 4f imaging platform integrated with a microfluidic channel to identify and sort single droplets of volume ∼0.5 pL. They constructed a modular setup using a 4f imaging system with a 4× objective to measure the spectra from a train of droplets. In particular, they showed that the presence of index matching between the droplet and the oil could enable the measurement of around 75% of the plug-shaped droplets. Using this system, they showed the detection of gold nanoparticles (spherical and nanorods), as well as DNA-mediated dimer formation within the droplets (no chemical reactions). They showed a detection limit of 6 AuNP/droplet, and a temporal time resolution of 2 ms, which could be further improved to 500 μs with a lower S/N ratio.[34]

It should be noted that the NA of the objective decides the angular range of the collected forward-scattered signal. Therefore, by tuning the NA of the collection objective, it is possible to measure either the extinction signal (low NA) or a convolution of extinction and scattered signals (high NA). Both Probst *et al.* and Sulliger *et al.* have tailored the continuous phase,[33,34] by using a fluorinated oil of higher absorbance in the former and an index-matched oil in the latter, to improve the S/N ratios, which is typically not feasible in many cases involving chemical reactions (inert oil is preferred). Hence, it is prudent to study systems where there is non-negligible scattering from the droplet edges in the context of single-droplet measurements.

In addition, when dealing with chemistries in droplets, the channel geometry, channel material, choice of continuous phase and flow rate ratios between the continuous and dispersed phase play an important role. Typical geometries employed for microfluidic droplet generation are the "flow focusing" and/or "T-junction geometries" in traditional PDMS-based microfluidics.[35] The sizes of the aqueous droplets of the dispersed phase formed in the continuous oil phase in these geometries are modified by varying the flow rates of the two fluids (oil and/or aqueous) with respect to each other. These variations in the flow ratios of the fluids alter the inertial forces, viscous forces and interfacial forces between the fluids given by the Reynolds number ($\mathrm{Re} = D\nu\rho/\mu$) and the capillary number ($\mathrm{Ca} = \mu\nu/\sigma$), where $\nu$, $\mu$ and $\rho$ are the velocities, viscosities and densities, respectively, of either the continuous fluid or dispersed fluid depending on the fluid considered in the evaluation, $D$ is the characteristic dimension of the microchannel and $\sigma$ is the interfacial tension between the two fluids. The opposing viscous shear and interfacial forces between the continuous and advancing dispersed phases lead to droplet breakup at the junction.[36,37] For example, spherical droplets of varying dimensions are typically formed in a flow focusing junction where the narrow necking geometry contributes to the droplet formation in addition to the favourable Re and Ca. This geometry is preferred only in the case of slow reactions, requiring high frequency droplets as in the case of droplet polymerase chain reaction (dPCR),[38] organoids and spheroids for 3D cultures and bioassays that look at large volume collection and monitoring over a period of time.[39,40] These geometries are generally not suitable for kinetically-controlled chemical reactions, as such reactions typically lead to fouling and flow disruption at the narrow necking junction. This effect is also shown in Fig. S1 of the (SI, details in the "Droplet generation in the microfluidic chip" section of Materials and Methods).

T-junction geometries have orthogonal channels where the dispersed phase meets the continuous phase flowing along a long primary channel at a 'T'. The breakup mechanism involves only the interplay between the three above-mentioned forces represented in terms of Re and Ca, leading to droplets of varying shapes depending on the flow rate regimes, including spherical, bullet-shaped (with a narrow leading edge and a wider trailing edge), and capsule-shaped droplets (with wide leading and trailing edges), as well as other irregularly shaped droplets.[41–45] A T-junction is the preferred geometry for chemical reactions involving droplets and/or reactions involving material exchange between the dispersed and continuous phase and segmented flow.[39,40,46–49]

Given a particular geometry, the shape and size of the droplets are modified by changing the flow rates of the aqueous fluid ($Q_a$) and the continuous phase fluid/oil ($Q_o$), *i.e.* by adjusting their flow rate ratio, $R = Q_a/Q_o$. However, as the flow ratio is dependent on the final concentration of the reagents for reaction chemistry, the effective range of flow ratios that can be used without affecting the final concentrations in the droplets is, in most cases, very limited. Hence, the droplet shape is essentially process-dependent, which leads to the use of anisotropic droplet shapes in most droplet microreactors. Thus, for application-based droplet microflow processes, the droplet shape cannot be dictated by the analysis method, which implies that single-drop analysis methods need to cater to droplets of any shape and size.

This has also been highlighted by a recent work by Zanini *et al.*, where they explained the effects of light illumination on an ellipsoidal droplet in the squeezing, dripping–squeezing transition, and dripping regimes in rectangular channels, both experimentally and using theoretical simulations.[50] They then went on to show the best microfluidic configuration with high signal detection regions, emphasizing the fact that optical interrogation of spherical droplets significantly reduces the applicability of such methods to real processes. However, in their study, they used an in-plane optical interrogation through a waveguide illumination, which intrinsically leads to the droplet being illuminated with a divergent beam that has different light–droplet interactions. Furthermore, the in-plane illumination geometry severely limits the types of chips that can be integrated with this online platform.

In this article, we develop an approach for monitoring single droplets (bullet and capsule-shaped droplets formed in the T-junction geometry) by integrating a microfluidic droplet system with a customized optical setup developed in the lab. In particular, we measure the forward-scattered optical signal to study the evolution of signals arising from single droplets. In the first part of the article, we explain the developed platform and the associated data analysis used for extracting the single-droplet information. Subsequently, we employed this technique to study the presence of gold nanoparticles within single droplets. We also studied the *in situ* synthesis of gold nanoparticles to demonstrate the versatility of the proposed technique for the analysis of single droplets on the fly within microfluidic flow systems. This is the first demonstration of the optical interrogation of a single-droplet with a chemical reaction leading to the synthesis of gold nanoparticles.

## Materials and methods

### Materials

Sodium borohydride ($NaBH_4$, 98%), hydrogen tetrachloroaurate (III) trihydrate ($HAuCl_4 \cdot 3H_2O$, 99.99%), hexadecyltrimethylammonium bromide (CTAB, 99%), silver nitrate ($AgNO_3$, 99.9% of Ag) and L-(+)-ascorbic acid (AA, 99%) were purchased from SRL Co. Ltd Silicone oil (99%, viscosity of 10 cSt) was purchased from Taranath Scientific limited. Additionally, ultrapure deionized (DI) water with a resistivity of 18 MΩ m was used for all experiments. High-purity water was used to avoid contamination and was crucial in ensuring repeatable results.

### Microfluidic chip fabrication

SU-8 master patterns on silicon wafers were used as templates for PDMS (Sylgard 184, Kevin Electrochem, India) device fabrication. Briefly, the PDMS base and curing agent were mixed in a 10 : 1 ratio and poured over the master pattern, degassed and allowed to cure at 70 °C for 2 h The cured PDMS slab was then peeled off from the silicon template, inlet/outlet holes were punched, and the sample was cleaned and bonded to a PDMS coated glass slide after 40 s of plasma treatment (Harrick plasma PDC-32G-2, USA). Tubings (FEP, Vici, India) of inner and outer diameters 0.8 mm and 1.5 mm, respectively, were fixed to the inlet/outlet holes and glued using epoxy (Devcon, India). The microchannels used in this study were rectangular in cross-section and were 300 μm wide, 155 μm deep, and 4.5 cm long. The layout of the microfluidic chip is shown in Fig. S2 of the SI.

### Droplet generation in the microfluidic chip

As mentioned previously, we also used the flow focusing (FF) geometry of two different dimensions to generate droplets for gold nanomaterial synthesis, as shown in Fig. S1 of the SI. The dimensions of the narrow necking zone of the device in the images shown in Fig. S1A and B are 50 μm width and 150 μm length and depth, while those in Fig. S1C–F are 200 μm width and 200 μm length and depth. The continuous fluid (silicone oil) flows through channels marked 'oil' and the dispersed fluid (an aqueous solution of gold salt and ascorbic acid, the reducing agent), flows in through the inlets marked 'Aqueous'. Fig. S1A corresponds to the 'only water' experiment, which leads to isotropic droplets forming at the junction. For gold nanoparticle synthesis, gold salt (0.5 mM) and reducing agent (ascorbic acid at 0.5 M and 1 M, considered to be a slow reducing agent for gold salt), were flowed in through 2 different inlets, meeting just near the narrow neck. As can be seen in all the gold nanomaterial synthesis experiments (Fig. S1B–F), there are deposits on the channel, which leads to channel fouling and flow disruption. Hence, we use the T-junction geometry in this study.

In this study, we used a T-junction microfluidic device that comprises three inlets as shown in Fig. S2 of the SI. Silicone oil was pumped through inlet 1, and water through inlet 2 using a syringe pump (Chemyx, USA). The third inlet (GNR in Fig. S2 of the SI) was used for the experiments performed with gold nanorods only and was blocked for other experiments. The microfluidic chip was placed under a stereomicroscope (Nikon SMZ1270) and the droplets formed in the channel were imaged for different flow rates of oil and water. Table S1 of the SI lists the flow rates, corresponding velocities and flow ratios used in the experiments. The images were then processed using ImageJ to determine the dimensions of the generated droplets.

### Gold nanorod synthesis

Gold nanorods (GNR) were synthesized using the seed-mediated growth method proposed by Nikoobakht and El-Sayed.[51] Briefly, seeds were synthesized by adding freshly prepared ice-cold $NaBH_4$ (0.6 mL of 0.01 M) to a mixture of aqueous $HAuCl_4 \cdot 3H_2O$ (10 mL of 0.5 mM) and CTAB (10 mL of 200 mM) solution. The mixture was vigorously stirred for 2 min, until the colour of the solution turned brown, indicating the formation of seeds of size ~4 nm. Freshly prepared seeds were further used for the growth of GNRs by adding growth solution (1 mM $HAuCl_4$, 0.2 M CTAB and 4 mM $AgNO_3$) to 70 mL of AA (0.078 M). 12 mL of the freshly prepared seed solution was then added to the colourless solution and kept undisturbed for 20 min for the growth of the GNRs. The as-prepared samples were then characterized using UV-visible spectroscopy (Shimadzu UV-1780) and TEM (JEOL F200FS, operated at 200 KV).

### Modelling light scattering by droplets

The light scattering by single droplets was calculated using the ray tracing method.[52] Here, each aqueous droplet (refractive index of 1.33) was embedded in a homogeneous background of oil (refractive index of 1.45). The droplet was illuminated with a localized collimated light source mimicking the illumination conditions used in the experiments. The forward-scattered light was detected by a detector (with an angular range of 70°). Note that in the experiments, a 60× air immersion objective (NA of 0.7) was used, which corresponds to a collection angle of 44°. The positions of the illumination source and the detector were kept fixed, whereas the droplet was moved relative to them. This enabled us to study the changes in the forward scattering as the light from the source illuminates different parts of the droplet.

### Optical transmission spectroscopy

A homemade optical setup was used for all the real-time optical spectroscopic measurements. Briefly, the system consisted of an inverted optical microscope (Nikon Ti2U) coupled to an optical spectrometer (Andor Kymera 328i with Newton 920 CCD). The microfluidic chip was illuminated with a halogen light source through a condenser lens (NA of 0.52). The area of the light illumination was 0.5 $\mu m^2$. The condenser aperture was tuned to choose the illuminated region of the droplet. The transmitted light was collected using a 60×, 0.7 NA air immersion objective and analysed by the spectrometer. The spectrometer could acquire a spectrum with 3 ms acquisition time and was operated at 3 MHz rate to acquire the maximum number of spectra from a given droplet. The spectrometer acquisition parameters, like integration time, repetition rate and clock speed, were adjusted such that maximum data throughput for a single droplet was achieved. It should be noted that this is primarily limited by the dark current and the noise level of the CCD in the spectrometer. For a droplet with a length of 600 μm, an integration time of 3 ms ensures that over a period of 30 s cumulative time, we acquire 8200 spectra and measure the spectra from 25 distinct droplets. A similar trend is expected for droplets with smaller dimensions ($\approx$40 μm) as well.

### Data analysis

We recorded ~5000–8000 spectra for a single flow condition, using the customized optical spectroscopy setup. Each spectrum was recorded with a 3 ms acquisition time. The relative transmission intensity was derived by normalizing the raw spectrum with the spectrum from the bulk PDMS chip (without the flow channel). The dark current was subtracted from each of the raw spectra and the reference spectrum prior to normalization. Subsequently, the data was analysed using a MATLAB code that allowed us to first highlight the regions of high modulation in the relative transmission spectrum. This corresponded to the edges of the droplets. Using the information of the droplet edges, the time points corresponding to the droplet region and oil region were identified. It should be noted that through this analysis, we get the normalized transmission intensity as a function of wavelength and time.

## Results and discussion

In this work, we demonstrate the light interaction with anisotropic nanoparticles in non-spherical droplets using homemade optical spectroscopy, which enables real-time, non-invasive monitoring with high sensitivity. As mentioned earlier, isotropic droplets are typically formed using microfluidic flow focusing geometries and require fluids to pass through a narrow neck, as shown in Fig. S1A of the SI. As shown, oil flowing through the channels marked '*a*' and '*b*' focuses the water flowing in from the inlet marked '*c*' through a narrow (50 μm) channel. For reactors containing reagents, this neck serves as a rapid diffusion zone for instantaneous reactions leading to uncontrolled fouling and flow disruption (Fig. S1B, SI). Hence, most drop-based chemistries prefer T-junction geometries, where there are no narrow channels to enable droplet breakup, and the so-formed droplets need not be isotropic, as shown in Fig. 1. The ellipsoidal (almost isotropic) droplets in Fig. 1A were generated in our flow focusing microchannel, while the anisotropic droplets shown in Fig. 1B and C were generated in T-junction microchannels with $R = 0.5$ and 1.2,

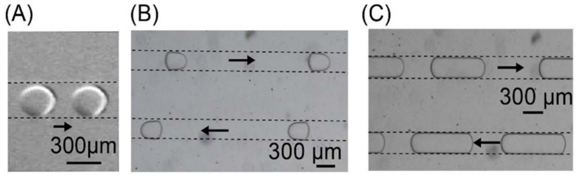

Fig. 1 Stereomicroscopic images of (A) Ellipsoidal droplets formed in the flow-focusing geometry with $R = 1$. (B) Bullet-shaped droplets formed in the T-junction geometry with $R = 0.5$. (C) Capsule-shaped droplets formed in the T-junction geometry with $R = 1.2$.

respectively. We also observed that the bullet-shaped droplets were not formed for $R > 0.75$. The nature of the breakup at the junction is determined by the flow ratios of the fluid in question, and the channel geometry also dictates the size and shape of the droplets formed (which essentially shows that the droplet shape is process-dependent). Hence, we had no control over the shape of the droplets formed during our nanoparticle synthesis within droplets.

## Light scattering from single microfluidic droplets

Fig. 2A shows a schematic of the numerical modelling of light scattering by a droplet with an ideal cylindrical shape with hemispherical caps (blue). The forward-scattered intensity is affected by the portion of the droplet illuminated by the light source. In the case where the extremities of the droplet are illuminated, refraction of light due to various incidence angles (with the surface) leads to significant scattering at high angles, and less intensity is directly transmitted. Fig. 2B shows the light scattering intensity as a function of scattering angle and relative droplet position. This shows that when light is positioned at the ends of the droplets, light is scattered significantly. It is clear that only some of the scattered light can be collected, which corresponds to the limits imposed by the NA of the collection objective. Fig. 2C shows the images of light scattering for different positions of the droplets.[52] In the case where the beam diameter is smaller than the droplet size ($I_L << L$), light scattering from the edges can be prominently observed by measuring the forward scattered light. Additionally, once the beam traverses the curved ends of the droplet, the light scattering is minimal at higher angles, enabling monitoring of the different parts of the droplet. On the contrary, in the case where the beam diameter is comparable to the droplet size ($I_L \sim L$), the measured signal in the forward scattered direction is a convolution of the signal scattered from the edges and from the flat part of the droplet. This condition would provide an averaged signal from a single droplet, and information about the spatial variation of the signal is lost. From these analyses, it is clear that a judicious choice of the illumination as well as the collection conditions is crucial for performing single-droplet optical spectroscopic analysis. In the following sections, we use a homemade optical platform for carrying out single-droplet measurements. We used GNR as a representative system for validating the system.

## Measuring the response of single droplets

We performed flow experiments to analyse the droplet size with variations in $R$. Stereomicroscopic images taken using a Nikon SMZ1270 (Fig. 3A) were processed using ImageJ, and their non-dimensional length ($L/w$, $w$ being the channel width) was plotted against $R$ (Fig. 3B, with the insets showing a droplet). The $Q_a$, $Q_o$ and $R$ for the droplets in Fig. 3A were 3, 4 μL min$^{-1}$ and 0.75, respectively, thus leading to a capsule-shaped droplet of length ~1185 μm. As can be seen, as $R$ increases, typically $Q_a$

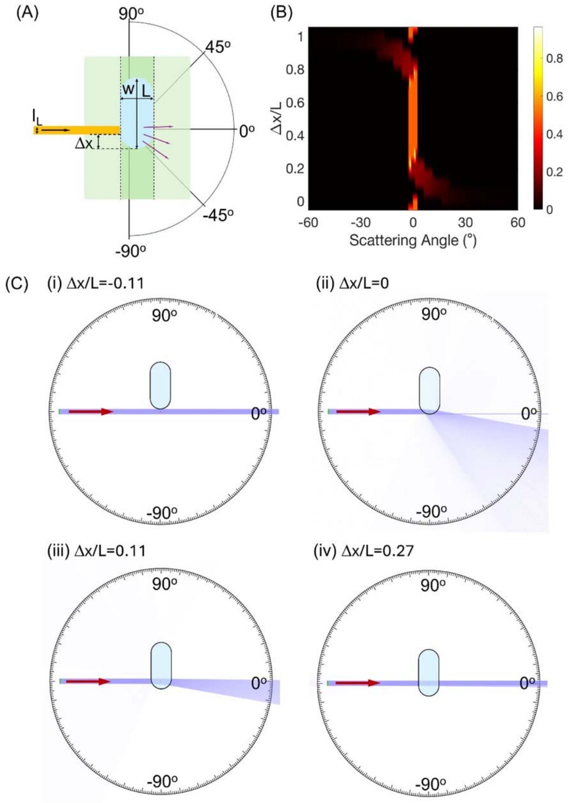

Fig. 2 (A) Schematic of the configuration used for understanding light scattering from single droplets. (B) Relative scattering intensity (color) as a function of scattering angle and relative position of the droplet ($\Delta x/L$). The beam size ($I_L$) and droplet width are kept fixed at 0.11 L and 0.44 L, respectively. (C) Images showing the position-dependent angular scattering of light by the single droplet.[52]

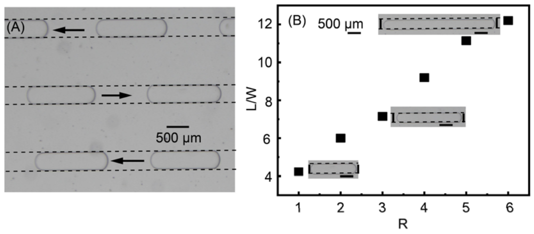

Fig. 3 Droplet analysis using a stereomicroscope. (A) Stereo microscopic image of droplets measured at a total flow rate of 7 μL min$^{-1}$ where $Q_a$ and $Q_a$ were 4 and 3 μL min$^{-1}$, respectively. (B) Various droplet sizes measured at different flow rates, where $L$ is the length of the droplet, $W$ is the width of the channel, and $R$ is the ratio of $Q_a/Q_o$; insets show representative images of the droplets.

increases for constant $Q_o$, and the volume of the droplets transitions from picolitres to nanolitres, thus leading to an increase in drop size – length. Thus, as the $R$ changes, the volume of the droplets and the final concentration of the reagents added into the droplets also changes. We then used similar flow ratios to perform optical measurements using the in-house-fabricated optical platform.

A schematic of the optical platform used for single-droplet measurements is shown in Fig. 4A. In this optical setup, we control the illumination and collection conditions. The condenser aperture is adjusted such that only a portion of the droplet is illuminated, limiting the volume from which the transmitted signal is collected. Furthermore, we use a 60× (0.7 NA) objective to collect both the directly transmitted light and forward-scattered light within a light cone of 44°. We placed the microfluidic device (Fig. 4A) between the objective and light source, on an adjustable ($x$, $y$, and $z$) stage, and the light illumination was on the droplet. Fig. 4B shows a schematic of the microchannel where the droplet breakup occurs at the T-junction geometry. Silicone oil (orange) flows through the first inlet while an aqueous solution of surfactant, (CTAB, at 0.5 mM, its critical micelle concentration, blue) was injected through the other two inlets representing the dispersed phase. The images of the droplets as captured using the inverted optical microscope camera, provided in Fig. 4C, show (i) the trailing edge, (ii) the drop centre and (iii) the leading edge of a single droplet.

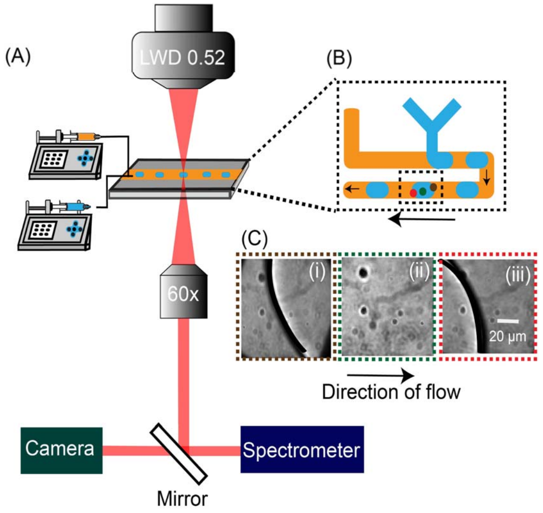

Fig. 4 (A) Schematic of the in-house optical setup used for single droplet spectroscopic measurements. (B) Schematic of the microfluidic T-junction chip used to form droplets. (C) Images obtained using the inverted optical microscope showing different locations of a single droplet highlighted in panel B. (i) The brown dot shows the trailing edge, (ii) the green dot shows the mid-section and (iii) the red dot shows the leading edge of the droplet.

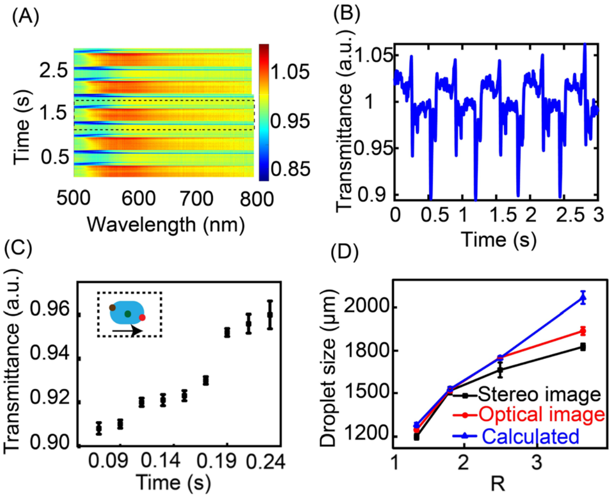

Fig. 5 (A) Droplet spectra plotted using MATLAB and (B) discrete droplet analysis, showing the transmittance plotted as a function of time at 665 nm. (C) Droplet transmittance profile plotted over time showing a distinct variation between the leading and trailing edges of the droplet using MATLAB data obtained from panel B. Inset shows the leading (red dot) and trailing edges (brown dot) on a single droplet. (D) Comparison of droplet size among the images obtained from stereo and optical microscopes, and through data analysis from optical measurements.

The captured raw data are shown in Fig. 5A, a typical spectral plot showing the variation in the normalized transmission intensity as a function of wavelength and time. Using MATLAB, we analysed the spectra acquired in each experiment. The spectral plot of the captured data provided in Fig. 5A can be interpreted as follows: the red regions of intensity $\sim$1.05 correspond to the edges of the droplets due to increased scattering at the droplet boundaries. The centre of the drop containing water is indicated by the green region, where the intensities go down to $\sim$0.95. The blue regions of intensities $\sim$0.85 represent the oil phase, where light scattering is less than that of the droplet region (both the edges and the centre). This is due to the change in the refractive index of the water (1.33, CTAB = 1.46) and oil (1.403).

Fig. 5B shows the transmittance intensities as a function of time for a fixed wavelength. Because of the dynamic state of the droplets, the scattering of light interaction by the droplets changes even under constant illumination throughout the experiment. This plot also shows the number of droplets generated within a 3 s window for a specific flow rate. First, the data set analysed was grouped to cluster the spectra originating from the droplet region ("droplets-only") or from the continuous phase ("oil only"). Due to large scattering at the oil-droplet interface, the transmitted signal depicts a large change in signal, which we attribute to the interface. Fig. 5B highlights the droplet and oil phase regions based on the system's transmittance levels. The transmittance value 1 represents the oil phase, and 1.04 and 1.05 depict the droplet preceding and leading-edge transmittance signals. This was confirmed by measuring the temporal cuts of the preceding and trailing edges of the droplet images from a stereomicroscope, as shown in Fig. S3 of the SI. The front end of the drop shows lower counts as compared to the back end of the drop, which directly corresponds to the lower transmission spectrum at the front end of the droplet. Comparing this to the spectral data, we are able to assign the orientation of the droplet (front and back) with the spectral time trace, *i.e.* on comparing Fig. 5C and S3B, at 0.05 s, the lower transmittance of ~0.9 corresponds to a drop dimension of ~60 μm, which is the leading front compared to the transmittance intensity (~0.96) at 0.24 s where the droplet dimension is ~150 μm, the trailing end of the droplet. In addition, we also compared the droplet lengths calculated from stereomicroscopic images (black, closed circle, Fig. 5D) and optical microscopic (red, closed circle, Fig. 5D) images. We also used the captured videos (1 s) from the microscopes and calculated the droplet lengths based on the velocity of the fluid and the elapsed time, represented as calculated (blue closed triangle). This comparison between the stereo and inverted optical microscope images for a given time and drop size ensured the accuracy of our analysis.

As previously mentioned, changing $R$ resulted in varying drop length 1.2 mm to 2 mm, when $R$ was varied from 1.3 to 3.4, respectively, as shown in Fig. 5D. All three obtained plots show minimal variations at low $R$, while the variations are significant at higher values of $R$ because of the error in measurements of high-speed videos. Hence, we restricted our range of $R$ to < 2 for further experiments. We hence performed experiments with a total flow rate of 4 μL min$^{-1}$ with both $Q_a$ and $Q_o$ equal at 2 μL min$^{-1}$; thus, the droplet size was maintained at ~600 μm across experiments. The total volume of the aqueous sample in each droplet under such conditions was 13 nL, while the light illumination corresponds to a volume of around 3.4 nL achieved by adjusting the condenser aperture.

### Analysis of GNR-loaded microdroplets

As we are now able to recognize the 'droplet only' regions in the obtained raw data, we went on to identify the presence of GNRs in the drops. To achieve this, we considered a series of total flow rates, *i.e.*, 1, 4, and 7 μL min$^{-1}$, while maintaining a constant droplet size (~600 μm) as in previous experiments by maintaining constant $R$ at 1 and equal $Q_o$ and $Q_a$ across all experiments.

We then measured the transmittance spectra for each droplet obtained from various total flow rates for a fixed wavelength region from 400–900 nm. Irrespective of the total flow rate, we obtained a flat transmission profile for water-containing droplets (Fig. S4 of SI). Subsequently, we performed similar experiments where the aqueous fluid was replaced with GNRs. These GNRs exhibit a longitudinal localized surface plasmon resonance (LSPR) peak at 665 nm with a strong absorbance of 1.6 a.u., as shown in Fig. 6A. A representative TEM image of the GNRs is shown in Fig. 6B, showing a nominal aspect ratio of 2.6 ± 1.3. As the GNRs exhibit a strong absorbance at 665 nm due to their LSPR, we were able to capture their signal effectively at all 3 total flow rates tested, as shown in Fig. S5, SI. However, we observed that lower flow rates (*i.e.*, reduced droplet velocity) produced significantly higher optical transmission signals compared to higher flow rates (*i.e.*, faster droplet velocity). This behaviour can be attributed to a decrease in the interfacial tension between the aqueous and oil phases, which is inversely proportional to the flow velocity. As the flow velocity increases, the interfacial tension decreases, leading to weaker scattering and absorption signals and signal clarity.[28]

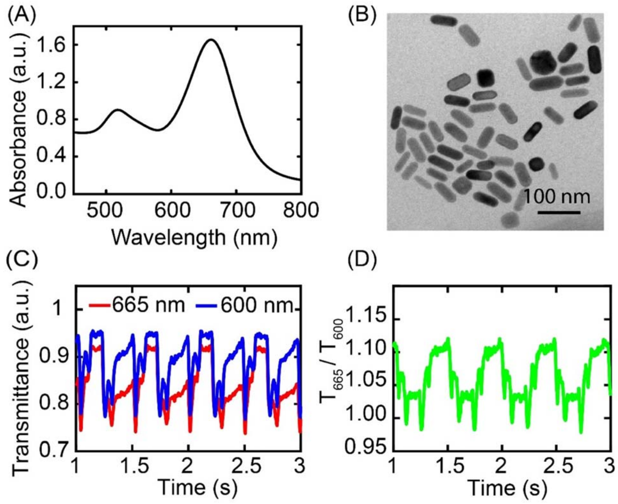

Fig. 6 (A) UV-visible absorption spectrum of the GNR exhibiting a longitudinal LSPR at 665 nm. (B) Representative TEM image of the GNRs. (C) Normalized transmission as a function of time at two different wavelengths, *i.e.*, at 665 nm (resonance wavelength of GNR) and 600 nm (off-resonance wavelength) for 3 s. (D) The transmittance ratio between the two wavelengths noted in panel C to identify the intensity variation in the oil phase and GNR-loaded droplet region.

Hence, we used an intermediate total flow rate of 4 μL min$^{-1}$ for further experiments.

To further quantify the GNR contribution, we considered two wavelength values: 665 nm, the resonance wavelength, and 600 nm, the off-resonance wavelength, and performed the comparative spectral analysis. The obtained transmittance as a function of time is shown in Fig. 6C, at 665 nm (red, resonant) and 600 nm (blue, off-resonance). The change in transmittance between two wavelengths in the 'droplet only' region is 0.08 (Fig. 6D), while the change in transmittance between the two wavelengths in the 'oil only' region is 0.02. This pronounced variation in transmittance between the two wavelengths in the 'drop only' region, compared to the 'oil only' region, indicates the presence of GNRs in the 'drop only' region, *i.e.* the optical signatures of the GNRs at 665 nm in the droplets, as opposed to their absence in the oil.

### Dilution of GNR concentration in a single droplet

After identifying GNRs in the 'drop only' region, we further performed dilution experiments to investigate the effects of varying GNR concentrations within individual droplets. We achieved this by adding water and GNRs into the droplets. These experiments were performed for the same flow conditions as in previous experiments with water in one of the inlets and GNRs in the other inlet for the dispersed phase, as shown in Fig. S2 of the SI. We first performed water-only experiments with the GNR inlet blocked and the water inlet at 2 μL min$^{-1}$, corresponding to a 0% GNR concentration. For subsequent measurements, the water flow rate was reduced to 1.5 μL min$^{-1}$, while the GNR flow rate was increased to 0.5 μL min$^{-1}$, corresponding to a 25% GNR concentration. The experiments were then conducted at 50%, 75%, and 100% GNR concentrations by adjusting the flow rates of water and GNRs while maintaining a constant droplet size across all experiments. The analysed data are shown in Fig. 7; Fig. 7A is a plot of the transmittance spectrum of a single droplet at various GNR concentrations. The blue line represents the baseline, 0% GNR concentration (*i.e.*, 100% water), resulting in a flat transmission profile. As the GNR concentration increased from 0% to 100%, a continuous shift in the transmittance spectrum was observed, with a notable increase in the depth of the transmittance at the longitudinal peak (665 nm), indicating the increasing transmittance of the GNRs within the droplet. This trend highlights the direct correlation between GNR concentration and transmittance changes. Fig. 7B depicts the average transmittance spectrum for all droplets in the experiment. This analysis revealed that there was minimal variation between the individual droplet measurements and the average values across all droplets. The average values, calculated from data analysis of all the droplet data, confirm the overall trends observed in single droplets, but smooth out the variations between droplets, providing a broader view of the effects of GNR concentration. In Fig. 7C, we present the comparison between the average and the single-droplet transmittance data. This comparative analysis further confirms that the transmittance changes are primarily due to the presence of GNR particles within the droplets, and it quantifies the spectral shift across different GNR concentrations. We then plotted the S/N line on this curve (black dotted line) in order to determine the limit of detection of our system. The S/N was measured and averaged across all the single-droplet transmittance data, and the limit of detection (LoD) of our system was determined to be the GNR dilution at which the S/N intersected the change in transmittance (∼13%), corresponding to a GNR concentration of $8.3 \times 10^8$.

## Real-time monitoring of *in situ* synthesis of gold nanoparticles within droplets

We conducted a detailed analysis of gold nanoparticle synthesis through single-droplet measurements using two distinct cases of experiments. In the first case, we examined spatial effects by shifting the droplet's position by a few centimetres to monitor *in situ* changes during the reaction. In the second case, we investigated the impact of varying reactant concentrations within a single droplet at a fixed location along the channel. We have included a third case where we try to analyse the data obtained from similar experiments using a FF geometry (as shown in Fig. S1A–F). To mitigate the fouling issues associated with this geometry, a T-junction configuration was preferred for the synthesis of gold nanoparticles.

### Case 1: influence of measurement location on the synthesis of gold nanoparticles (GNPs)

For the first set of experiments, the microfluidic device was configured with two inlets for the dispersed phase: one for the gold precursor solution and one for ascorbic acid (1 M of AA) as shown in Fig. S6A of the SI. Upon convergence of the gold precursor and ascorbic acid streams into the droplet, rapid mixing led to reaction and formation of GNPs almost instantaneously. The first measurement was taken at the T-junction where droplets are formed, marked P1 in Fig. 8A, and the second was taken downstream (∼2.7 cm length of the channel), at location P2, in order to observe the changes over time. We measured the spectral transmission from a single droplet as well as calculated the average transmission over 15 drops, as shown in Fig. 8B and C. Note that the transmission dip at 523 nm indicates the formation of spherical GNPs, and the intensity is proportional to the concentration of GNPs.

Fig. 8B shows a dip of 0.65 a.u. at 523 nm, indicating a lower concentration of GNPs at location P1 (pink). At location P2 (blue), the transmission of the droplet is lower (∼0.51 a.u.), showing a prominent dip, indicating a higher density of particles. This significant increase in absorbance (decrease in transmittance in Fig. 8B) at location P2 confirms the progressive nanoparticle growth within the moving droplets as the droplets traverse the channel. This spatial difference underscores the effectiveness of our microfluidic approach in capturing the real-time evolution of nanoparticle synthesis. A comparison of Fig. 8B and C indicates that both single-droplet spectra and average spectra show similar variations in the transmission intensity.

### Case 2: variation in the concentration of AA

To demonstrate that this technique is able to track changes in the nanoparticle synthesis, we performed the real-time

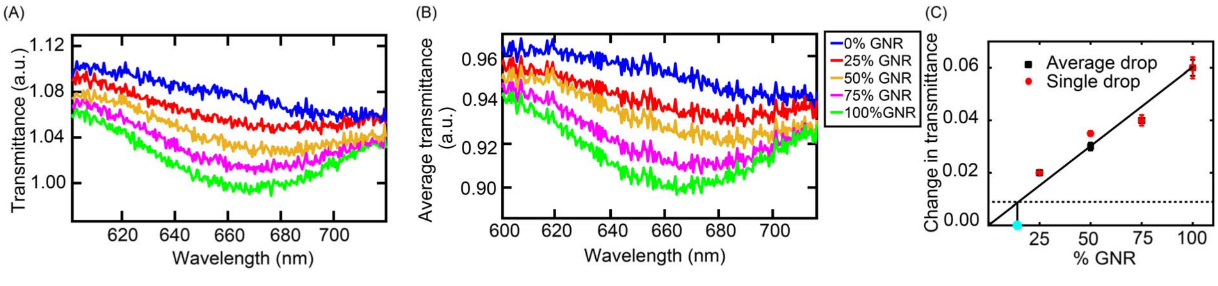

Fig. 7 Dilution series of anisotropic gold nanoparticles: plots showing: (A) transmittance as a function of wavelength as the concentration of GNRs varies in a single droplet. (B) Transmittance *vs.* wavelength averaged across 28 droplets (8200 spectra) by eliminating the oil phase using MATLAB code. (C) The change in transmittance for the GNR dilution obtained using both single droplet analysis and average droplet analysis. The dotted line represents the signal to noise ratio measured and averaged across all the single drop transmittance data, which intersects the trendline (black line) at the least GNR dilution that can be detected using our system – the blue dot at 13% GNR represents the limit of detection of our system.

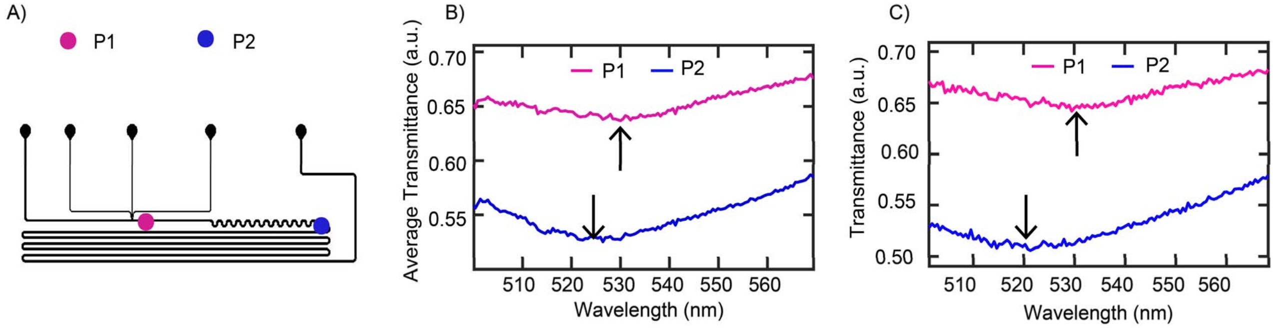

Fig. 8 Influence of measurement location on the synthesis of gold nanoparticles (Case 1): (A) schematic of the microfluidic T-junction device showing 2 locations P1 and P2, where spectral measurements were taken, to indicate the formation of gold nanoparticles. Plots of (B) transmittance as a function of wavelength in a single droplet and (C) transmittance as a function of wavelength as the formation of gold nanoparticles varies averaged over all droplets.

measurements at a fixed location along the channel length for two different concentrations of the reducing agent (AA). The microfluidic device was configured with three inlets for the dispersed phase: one for the gold precursor solution, one for ascorbic acid (1 M of AA), and a third for water, which was either open or closed depending on the experimental requirement, as shown in Fig. S6B of the SI.

We measured the transmission spectra at the T-junction as shown by the black dot in Fig. 9A. We started with 1 M AA concentration (blue in Fig. 9B), and the measured spectra exhibit a dip at 535 nm (~0.76 a.u.). Subsequently, we introduced water through the third inlet to tune the AA concentration to 0.5 M, and the spectral signature is shown as pink in Fig. 9B. A higher transmittance value of ~0.85 a.u. at a peak wavelength of 535 nm at lower AA concentration indicates the formation of gold nanoparticles, albeit at lower concentration due to the low availability of the reducing agent, *i.e.* for lower concentrations of AA, the reduction of the gold salt is less, leading to a lower density of particles formed within the droplets. A clear difference in the reaction dynamics is observed due to the change in the concentration of AA. Furthermore, spectra from individual and averaged droplets show negligible differences indicating the uniformity of the particles synthesized in the train of droplets. Using these two cases, we demonstrate real-time measurements of on-chip synthesis of the gold nanoparticles with our in-house optical setup.

### Case 3: flow focusing device for GNP synthesis

We performed a few experiments using a flow focusing device shown in Fig. S1A within spherical droplets and tried to measure the transmission signals at the junction, where the droplets form. The spectral plot shown in Fig. S7A, indicates fouling in the channel (red), which results in improper identification of droplets *i.e.* the leading and trailing edge of the droplets were not differentiated correctly (Fig. S7B at 530 nm). Due to channel fouling, the drop edges could not be clearly defined.

The optical interrogation method developed here demonstrates that the optical response from single drops can be measured with high sensitivity even when there are no fluorescence or Raman markers within the droplets. Note that the measured contrast originates from the absorption of the gold nanorods and can be extended to any other system that exhibits absorption in the visible spectral region. Thus, this technique can potentially be used for all sorts of absorbing dyes, employed for biochemical assays, and other nanomaterials and nanoparticles.[53–55] The temporal resolution of this technique is limited by the data acquisition time of the spectrometer. The speed can be further increased by reducing the number of pixels of the CCD camera from which the integration is performed. Employing this, it is possible to record a spectrum every 30 μs. However, this reduction in the acquisition time also leads to a reduction in the S/N ratio of the acquired spectrum. Thus,

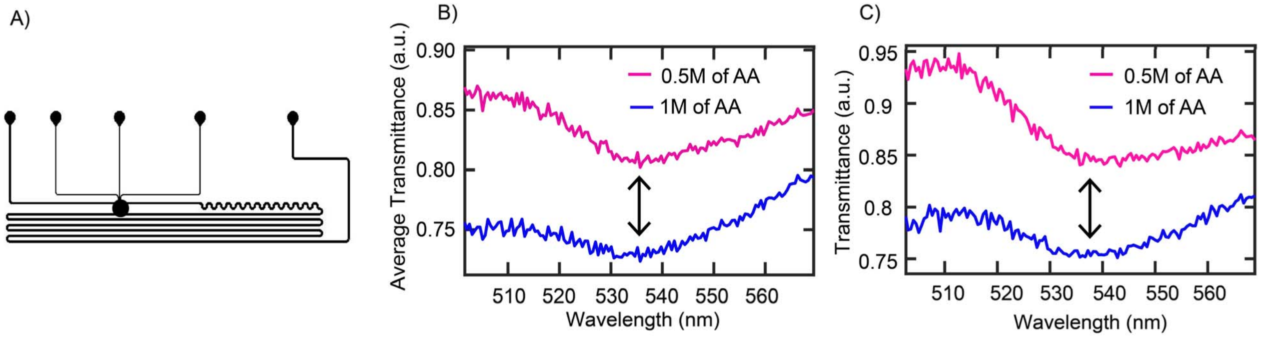

Fig. 9 Variation in the concentration of AA (Case 2): (A) schematic of the microfluidic T junction device showing the location at which the spectral measurements were taken, to indicate the formation of gold nanoparticle. (B) and (C) Plots of transmittance as a function of wavelength as the formation of gold nanoparticles varies (B) averaged over all drops and (C) in a single drop.

depending on the expected modulation of the absorbance in an experiment, a judicious choice of the integration time per spectrum and the S/N needs to be made. Furthermore, light sources with different wavelengths (for example, in the UV range) can be used for looking at proteins and DNA within single droplets and have potential implications for real-time single-droplet PCR analysis.[56–59]

## Conclusions

In conclusion, we developed a technique for single-droplet analysis using an in-house custom-built optical transmission spectroscopy setup integrated with a 'T' junction-based droplet microfluidic device. Using the understanding of light scattering from the droplets, we employed a MATLAB code to analyse the 5000–8000 spectra from a single flow condition and identify the spectra corresponding to the 'droplet only' region. We compared the stereomicroscopic images and optical microscope images to validate the 'drop only' and 'oil only' regions identified by spectral data analysis. We then interrogated individual droplets loaded with gold nanorods and measured their transmission spectral signatures. We also varied the concentration of AuNRs within the droplets to demonstrate the sensitivity of the single-drop measurement. On comparing the single drop data with the multi-drop averaged data, we showed that the signatures of the nanorods were retained even for single-droplet analysis; however, the S/N ratio was improved on averaging. Finally, we demonstrated the real-time monitoring of the *in situ* synthesis of gold nanoparticles within a single droplet. We showed that by varying the location of measurement along the channel length, it is possible to track the reaction timeline. We also showed the influence of reactant concentrations on the nanoparticle synthesis at a fixed position, vis-à-vis, a fixed reaction time. We envision that the established method could be used for *in situ* monitoring of most chemial and biochemical assays, exhibiting a change in the transmission signal of the solution within a single droplet over a wide spectral range.

## Author contributions

R. P. carried out the experiments, prepared the manuscript, and assisted in the discussions; J. P. assisted in the experiments and assisted in manuscript preparation; S. D.-G. and S. D. jointly conceived the idea, assisted in manuscript preparation, and assisted in the discussions.

## Conflicts of interest

The authors have no known conflicts of interest concerning the publication of this research.

## Data availability

The data supporting this article have been included as part of the supplementary information (SI). Supplementary information: Fig. S1: Drop generation and plasmonic nanomaterial synthesis in flow focussing devices. Fig. S2: T junction device used in this study. Fig. S3 :Droplet variation studies using stereo and optical microscopy. Fig. S4: Comparison of transmittance at resonance and off-resonance wavelengths. Fig. S5: GNR transmission with velocity. Fig. S6: Chip design for gold nanoparticle synthesis. Fig. S7: Spectral plot of fouled device. Table S1: Flow rate details of Fig. 3B. See DOI: https://doi.org/10.1039/d5na01087j.

## Acknowledgements

The authors would like to acknowledge financial support from the Ministry of Education granted to RP, the Seed research grant from Indian Institute of Technology Hyderabad (IITH/Seed Grant/2020-2021/F222/SG17) and the Start-up research grant from SERB-SRG (SRG/2021/001623) granted to SD. SDG would like to acknowledge funding support from the TDG Grant of IIT Hyderabad (TDG/IITH/F199/2024-25/TDG-08), SERB Ramanujan Grant (SB/S2/RJN-126/2017) and DST Nanomission Grant (DST/NM/NB/2018/118).

## References

1 H. Song and R. F. Ismagilov, *J. Am. Chem. Soc.*, 2003, **125**, 14613–14619.
2 B. J. Hindson, *et al.*, *Anal. Chem.*, 2011, **83**, 8604–8610.
3 Y. Schaerli and F. Hollfelder, *Mol. BioSyst.*, 2009, **5**, 1392.
4 R. L. Hartman and K. F. Jensen, *Lab Chip*, 2009, **9**, 2495.
5 T. Moragues, D. Arguijo, T. Beneyton, C. Modavi, K. Simutis, A. R. Abate, J.-C. Baret, A. J. deMello, D. Densmore and A. D. Griffiths, *Nat. Rev. Methods Primers*, 2023, **3**, 32.
6 S. Sart, G. Ronteix, S. Jain, G. Amselem and C. N. Baroud, *Chem. Rev.*, 2022, **122**, 7061–7096.
7 Y. Yang, C. Li, J. Kameoka, K. H. Lee and H. G. Craighead, *Lab Chip*, 2005, **5**, 869.
8 S. Li, C. Zhang, S. Wang, Q. Liu, H. Feng, X. Ma and J. Guo, *Analyst*, 2018, **143**, 4230–4246.
9 B. Kuswandi, M. Nuriman, J. Huskens and W. Verboom, *Anal. Chim. Acta*, 2007, **601**, 141–155.
10 Y.-J. Wei, Y.-N. Zhao, X. Zhang, X. Wei, M.-L. Chen and X.-W. Chen, *TrAC, Trends Anal. Chem.*, 2023, **158**, 116865.
11 Y. Liu, Z. Fan, L. Qiao and B. Liu, *TrAC, Trends Anal. Chem.*, 2022, **157**, 116822.
12 Z. Fattahi and M. Hasanzadeh, *TrAC, Trends Anal. Chem.*, 2022, **152**, 116637.
13 J. Pillanagrovi and S. Dutta-Gupta, *Nano Futures*, 2024, **8**, 045001.
14 E. Mukherjee, J. Pillanagrovi, D. Bhatnagar and S. Dutta-Gupta, *J. Appl. Phys.*, 2023, **133**(7), DOI: 10.1063/5.0132791.
15 S. Dutta-Gupta, N. Dabidian, I. Kholmanov, M. A. Belkin and G. Shvets, *Philos. Trans. R. Soc., A*, 2017, **375**, 20160061.
16 J. Pillanagrovi and S. Dutta-Gupta, *Nanotechnol*, 2022, **33**, 485301.
17 G. Kelp, J. Li, J. Lu, N. DiNapoli, R. Delgado, C. Liu, D. Fan, S. Dutta-Gupta and G. Shvets, *Lab Chip*, 2020, **20**, 2136–2153.
18 N. Dabidian, S. Dutta-Gupta, I. Kholmanov, K. Lai, F. Lu, J. Lee, M. Jin, S. Trendafilov, A. Khanikaev, B. Fallahazad,

E. Tutuc, M. A. Belkin and G. Shvets, *Nano Lett.*, 2016, **16**, 3607–3615.

19 J. P. Neto, A. Mota, G. Lopes, B. J. Coelho, J. Frazão, A. T. Moura, B. Oliveira, B. Sieira, J. Fernandes, E. Fortunato, R. Martins, R. Igreja, P. V. Baptista and H. Águas, *Lab Chip*, 2023, **23**, 3238–3244.

20 S. R. T. Neil, C. M. Rushworth, C. Vallance and S. R. Mackenzie, *Lab Chip*, 2011, **11**, 3953.

21 M. Li, F. Zhao, J. Zeng, J. Qi, J. Lu and W.-C. Shih, *J. Biomed. Opt.*, 2014, **19**, 111611.

22 H. Zhang, Y. Yi, C. Zhou, G. Ying, X. Zhou, C. Fu, Y. Zhu and Y. Shen, *RSC Adv.*, 2017, **7**, 52782–52793.

23 X. Casadevall i Solvas, X. Niu, K. Leeper, S. Cho, S.-I. Chang, J. B. Edel and A. J. deMello, *JoVE*, 2011, **58**, DOI: 10.3791/3437.

24 P. Gupta, A. Mohan, A. Mishra, A. Nair, N. Chowdhury, D. Balekai, K. Rai, A. Prabhakar and T. Saiyed, *Microsyst. Nanoeng.*, 2024, **10**, 35.

25 M. P. Cecchini, J. Hong, C. Lim, J. Choo, T. Albrecht, A. J. deMello and J. B. Edel, *Anal. Chem.*, 2011, **83**, 3076–3081.

26 M. P. Cecchini, A. Wiener, V. A. Turek, H. Chon, S. Lee, A. P. Ivanov, D. W. McComb, J. Choo, T. Albrecht, S. A. Maier and J. B. Edel, *Nano Lett.*, 2013, **13**, 4602–4609.

27 M. Srisa-Art, A. J. deMello and J. B. Edel, *Phys. Rev. Lett.*, 2008, **101**, 014502.

28 T. D. Rane, C. M. Puleo, K. J. Liu, Y. Zhang, A. P. Lee and T. H. Wang, *Lab Chip*, 2010, **10**, 161–164.

29 V. Srinivasan, V. K. Pamula and R. B. Fair, *Anal. Chim. Acta*, 2004, **507**, 145–150.

30 A. Zinchenko, S. R. A. Devenish, B. Kintses, P.-Y. Colin, M. Fischlechner and F. Hollfelder, *Anal. Chem.*, 2014, **86**, 2526–2533.

31 S. Hassan, A. M. Nightingale and X. Niu, *Anal*, 2016, **141**, 3266–3273.

32 T. A. Duncombe, A. Ponti, F. P. Seebeck and P. S. Dittrich, *Anal. Chem.*, 2021, **93**, 13008–13013.

33 J. Probst, P. Howes, P. Arosio, S. Stavrakis and A. deMello, *Anal. Chem.*, 2021, **93**, 7673–7681.

34 M. Sulliger, J. Ortega Arroyo and R. Quidant, *Anal. Chem.*, 2025, **97**, 2736–2744.

35 R. R. Pompano, W. Liu, W. Du and R. F. Ismagilov, *Annu. Rev. Anal. Chem.*, 2011, **4**, 59–81.

36 T. Thorsen, R. W. Roberts, F. H. Arnold and S. R. Quake, *Phys. Rev. Lett.*, 2001, **86**, 4163–4166.

37 A. Venkateshwarlu and R. P. Bharti, *J. Taiwan Inst. Chem. Eng.*, 2021, **129**, 64–79.

38 S. L. Anna, N. Bontoux and H. A. Stone, *Appl. Phys. Lett.*, 2003, **82**, 364–366.

39 A. Ghosh, S. Ghosh, F. Pati and S. Duraiswamy, *Bioprinting*, 2023, **36**, e00316.

40 S. ghosh, A. Ghosh, F. Pati and S. Duraiswamy, *ACS Biomater. Sci. Eng.*, 2025, **11**(11), 6684–6700.

41 Y. Mahdi and K. Daoud, *J. Dispersion Sci. Technol.*, 2017, **38**, 1501–1508.

42 A. Gupta and R. Kumar, *Phys. Fluids*, 2010, **22**(12), DOI: 10.1063/1.3523483.

43 S. Duraiswamy and S. A. Khan, *Small*, 2009, **5**, 2828–2834.

44 S. K. Jena, T. Srivastava, S. S. Bahga and S. Kondaraju, *Phys. Fluids*, 2023, **35**(2), DOI: 10.1063/5.0134087.

45 W. Han and X. Chen, *J. Braz. Soc. Mech. Sci.*, 2021, **43**, 247.

46 A. Gupta and R. Kumar, *Microfluid. Nanofluid.*, 2010, **8**, 799–812.

47 S. A. Khan and S. Duraiswamy, *Lab Chip*, 2009, **9**, 1840.

48 Z. Barikbin, Md. T. Rahman, P. Parthiban, A. S. Rane, V. Jain, S. Duraiswamy, S. H. S. Lee and S. A. Khan, *Lab Chip*, 2010, **10**, 2458.

49 S. Duraiswamy and S. A. Khan, *Nano Lett.*, 2010, **10**, 3757–3763.

50 L. Zanini and C. Sada, *Phys. Fluids*, 2023, **35**(3), DOI: 10.1063/5.0138475.

51 B. Nikoobakht and M. A. El-Sayed, *Chem. Mater.*, 2003, **15**, 1957–1962.

52 *Ray Optics Simulations*, 2025, https://phydemo.app/ray-optics/.

53 S. Hengoju, O. Shvydkiv, M. Tovar, M. Roth and M. A. Rosenbaum, *Biosens. Bioelectron.*, 2022, **200**, 113910.

54 E. Y. Basova and F. Foret, *Anal*, 2015, **140**, 22–38.

55 C. Ma, Z. Gao, J. Zhao and S. Feng, *NPE*, 2023, **6**(3), DOI: 10.1063/10.0019677.

56 Y. Hou, S. Chen, Y. Zheng, X. Zheng and J.-M. Lin, *TrAC, Trends Anal. Chem.*, 2023, **158**, 116897.

57 N. R. Beer, B. J. Hindson, E. K. Wheeler, S. B. Hall, K. A. Rose, I. M. Kennedy and B. W. Colston, *Anal. Chem.*, 2007, **79**, 8471–8475.

58 W. Zhang, L. Cui, Y. Wang, Z. Xie, Y. Wei, S. Zhu, M. Nawaz, W.-C. Mak, H.-P. Ho, D. Gu and S. Zeng, *Biosens. J.*, 2023, **14**, 2.

59 M. Born and E. Wolf, *Principles of Optics*, Cambridge University Press, 1999.